# Science

**MAAAS**

## Supplementary Materials for

## Exceptional fracture toughness of CrCoNi-based medium- and high-entropy alloys at 20 kelvin

Dong Liu *et al*.

Corresponding author: Robert O. Ritchie, roritchie@lbl.gov

**The PDF file includes:**

Materials and Methods
Figs. S1 to S7
References

## Materials and Methods

Materials Synthesis and Processing

Following the process described in earlier papers [52], equiatomic CrMnFeCoNi and CrCoNi alloys were produced from high-purity elemental starting materials (>99.9% pure) by arc-melting and drop-casting in an argon atmosphere into rectangular cross-section copper molds measuring approximately 25.4 mm by 19.1 mm by 127 mm. Castings of both alloys were homogenized at 1200°C for 24 h *in vacuo*, cut in half length wise and then cold forged and cross-rolled at room temperature to achieve plates with a thickness of ~10 mm. These sections were annealed in air at 800°C for 1 h to generate a fully recrystallized, equiaxed grain structure with an average grain size of ~21 μm in CrMnFeCoNi and ~8 μm in CrCoNi.

Sample Preparation

Compact-tension (C(T)) samples were machined from the recrystallized plates. For the CrCoNi alloy, C(T) samples of width, $W$ = 18 mm and thickness, $B$ = 5 mm, were prepared by electrical discharge machining (EDM) in accordance with ASTM standard E1820 [17]. For the CrMnFeCoNi alloy, the same procedures were adopted except that the sample thickness, $B$, was 9 mm. In both types of samples, notches ~6.3 mm in length with a root radius of ~100 μm were introduced by EDM. Fatigue pre-cracking was performed on all samples at room temperature using a servo hydraulic MTS 810 load frame (MTS Corporation, Eden Prairie, MN, USA) with an Instron 8800 digital controller (Instron Corp., Norwood, MA, USA). These fatigue cracks were introduced by tension-tension loading under load control at a $\Delta K$ of ~15 MPa.m$^{\frac{1}{2}}$, at a load ratio, $R$ = 0.1, and at a constant frequency of 10 Hz (sine wave). Crack extension was monitored by mounting an Epsilon clip gauge (Epsilon Technology, Jackson, WY, USA) with a 3 mm (-1/+2.5 mm) gauge length, at the load line of the specimen. Optical microscopy was used to inspect the crack length from both sides of the sample to ensure a straight crack front. The final crack lengths were no less than 9 mm in length with an approximate $a/W$ of 0.5 to ensure a pre-crack length well above the minimum length (~1.3 mm) required by ASTM E1820 [17].

For uniaxial tensile testing, cylindrical dog-bone shaped samples of the CrCoNi and CrMnFeCoNi alloys with a gauge-section diameter of 6 mm and a gauge length of 23.5 mm were machined from the 10-mm thick recrystallized plates.

Experimental Mechanical Testing Setup

Tensile and fracture toughness testing of both alloys at 20 K was performed at ENGIN-X, the dedicated materials engineering beamline at the ISIS Neutron and Muon Source at the Rutherford Appleton Laboratory at Harwell campus, Oxfordshire, in the U.K.. Nonlinear elastic fracture mechanics methodologies were employed to determine the fracture toughness in terms of crack-resistance $J_R$ curve, representing the change in crack resistance with increasing crack extension in the pre-cracked C(T) samples. These samples were loaded under displacement control at ~2 mm/min with a periodic unloading sequence (unloading compliance) adopted to determine the crack extension, $\Delta a$. Unloading was controlled by a Python script in which the load was reduced by ~10% at each unloading cycle, and the unloading compliance measured using the Epsilon clip gauge. Uniaxial tensile testing was performed at ~20 K using a crosshead displacement rate of 0.0235 mm/min.

At ENGIN-X, a unique cryogenic testing chamber was used, the details of which are described elsewhere [53, 54]. Briefly, it consists of a vacuum vessel with aluminium windows to permit access for the incident and scattered neutrons (fig. S1). Two cryo-coolers were connected to the infrared radiation shield of the chamber to control the temperature. The load, applied by an Instron 100 kN rated hydraulic frame with an Instron 8800 Controller, was transmitted to the sample by a shaft made from Ferralium 255 SD50 material and connected to a threaded section made from Inconel 718. Inside the chamber, the Inconel 718 shaft pulls into the CuBe pivot which is insulated by G10 cone and spacer (dielectric material with low thermal conductivity and high strength). A CuBe adaptor shaft is locked in position with CuBe nuts on a link plate that is connected directly to the first stage of the cryogenic cooler; a schematic of the grips assembly is shown in fig. S2. The sample holder grips are thermally linked through a copper clamp and a stack of laminated copper sheets for better conductivity.

A set of CuBe sample holder with CuBe pins were designed and installed to the cold fingers (fig. S3a). Two rhodium-iron temperature sensors: one on the CuBe cold fingers and the other one screwed to the bottom of the sample away from the crack tip (fig. 3b). The testing of the samples was conducted once the temperature sensor readings stabilised around ~10-15 K at the cold fingers and ~25-30 K at the bottom of the samples. Therefore, it is reasonable to take the average temperature from these temperature sensor readings as the temperature at the crack tip, namely, around 17.5-22.5 K. We approximate this as 20 K in the text.

For both alloys, one sample of each was tested *in situ* during neutron diffraction measurement. An additional three samples of each were tested *ex situ* to repeat the experiment and one more sample of each alloy was tested for comparison at room temperature (293 K).
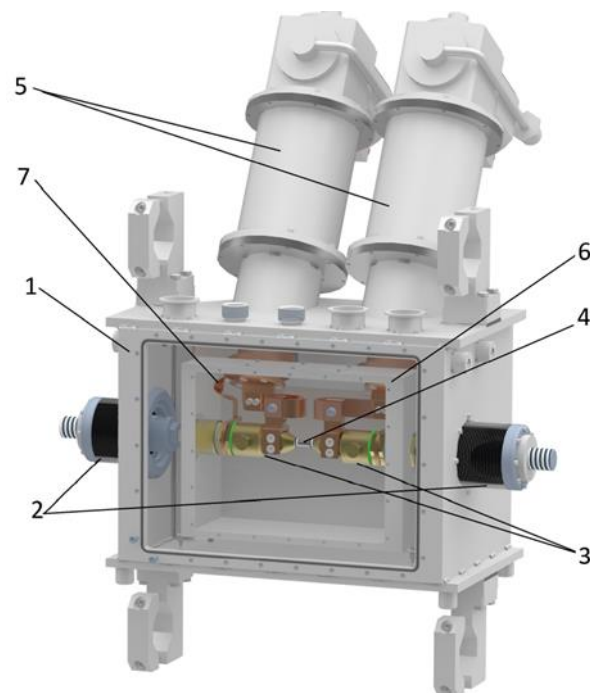


**Fig. S1**. **Schematic illustration of the ENGIN-X cryogenic testing chamber**: (1) outer vacuum vessel; (2) two bellow sections; (3) sample grips; (4) sample; (5) two cryo-coolers; (6) infrared radiation shield; (7) copper braids [53].
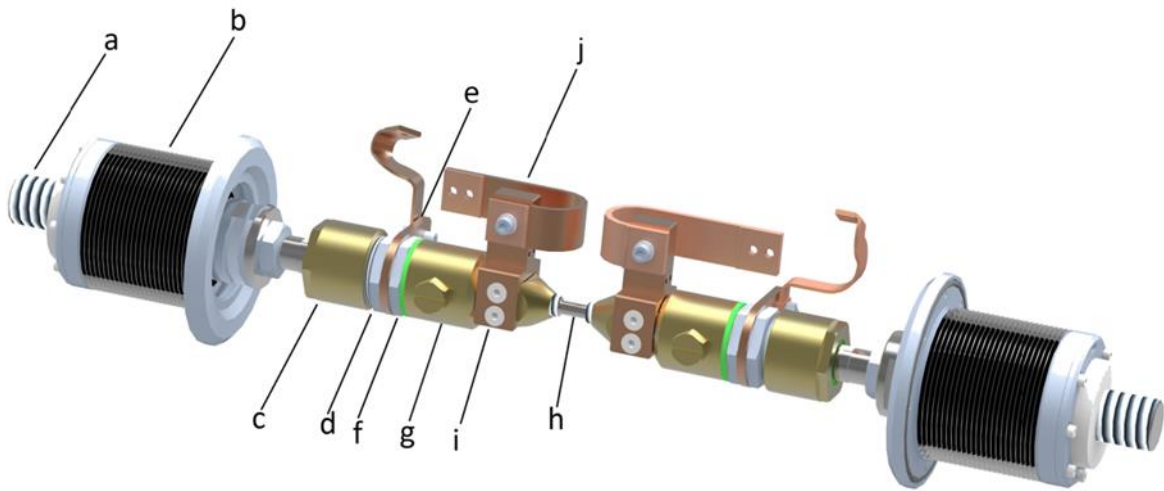
**Fig. S2. A detailed view of the grips assembly:** (a) shaft; (b) bellow section; (c) copper pivot; (d) adaptor shaft; (e) copper link; (f) G10 spacer; (g) copper-beryllium sample grip; (h) sample; (i) copper clamp; (j) stack of laminated copper sheets [53].
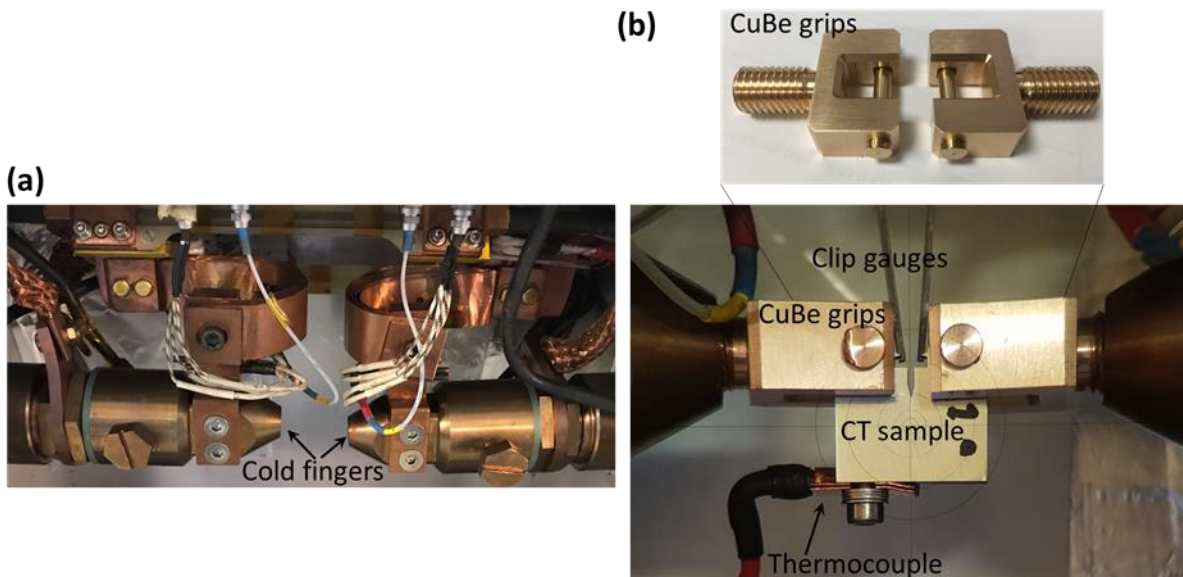


**Fig. S3. Further details of the specimen gripping assembly:** (a) A close-up view of the grips assembly. The samples are loaded between the cold fingers. (b) Photograph showing the set-up of the clip gauge, CuBe grips, the C(T) samples held by CuBe pins and a temperature sensor installed at the bottom face of the C(T) sample.

As ISIS is a time-of-flight (ToF) neutron spallation source, at the ENGINX beamline a high flux neutron beam with narrow pulse width is available with a 50 m primary flight distance ($L_1$) to the test specimen. It has two collimated detectors 180° ($2\theta$) apart at 90° and -90°, respectively, to the incident neutron beam. An instrumental gauge volume (IGV) located inside the C(T) specimen ahead of the crack tip was used to measure at about 4 x 4 x 4 mm$^3$. The distance between the IGV and the detectors was 1.53 m (the secondary neutron flight length, $L_2$). The detected neutron wavelength, $\lambda$, and the measured flight time, $t$, are related by:

$$\lambda = \frac{h}{m(L_1+L_2)}t \quad , \tag{1}$$

where $h$ is Planck's constant, and $m$ is neutron mass. As such, the ToF spectrum can be converted to a diffraction pattern with each peak corresponding to a family of {$hkl$} planes. The spacing of the crystal lattice planes, $d_{hkl}$, can be derived by:

$$d_{hkl} = \frac{h}{2sin\theta m(L_1+L_2)}t_{hkl} \quad , \tag{2}$$

where $\theta$ is the half angle between the incident and scattered neutron beams ($\theta = 45°$ was used in the current setup). Prior to the measurements, a calibration process was performed on a standard CeO$_2$ powder sample.

All the neutron spectra collected were analysed using a single-peak fitting with a Pseudo Voigt profile (_i.e._, mixed Gaussian and Lorentzian) convoluted with a sharp-edged exponential on a linear background. The centroid of the fitted peak in $d$-spacing units was taken as the lattice spacing. One sample from each alloy was tested _in situ_ with 24 neutron spectra collected for each sample, first in a nominally load-free condition (50 N pre-load) from 293 K to 20 K, and then at increasing loading steps until final fracture at 20 K. The calculated $d$-spacings and the crystal lattice shrinkage with temperature were derived and are presented below.

Despite the fact that our TEM images did reveal limited evidence of the formation of the _hcp_ phase, our _in situ_ neutron diffraction measurements did not. Of note here is that He et al. [45] reported the formation of 4 vol.% of _hcp_ phase based on the (101) peak in neutron diffraction spectra collected from a uniaxial tensile specimen tested at 15 K with a strain between 14% and

30%. However, in the present work the highly strained volume ahead of the crack tip is at least an order of magnitude smaller compared with a uniaxial tension configuration. With a 4x4x4 mm³ instrumental gauge volume used in the neutron measurement, the small fraction of *hcp* phase most likely did not yield sufficient diffraction signal discernable in the overall spectrum.

Uniaxial Tensile Testing

Samples of CrCoNi and CrMnFeCoNi were tested at 20 K under displacement control at an engineering strain rate of $10^{-3}$ sec$^{-1}$; in the early stages of deformation (strains < 3%) this strain rate was reduced to $10^{-4}$ sec$^{-1}$. Displacements during tensile testing were measured using an Epsilon axial extensometer attached to the gauge section. The extensometer (Epsilon Technology, Jackson, WY, USA) is rated down to ~3 K. The obtained stress-strain curves and relevant tensile data are shown in fig. S4. The 0.2% yield strength, $\sigma_y$, and ultimate tensile strength, $\sigma_{UTS}$, for the CrCoNi alloy were ~740 MPa and ~1290 MPa and for the CrMnFeCoNi alloy ~580 MPa and ~1 GPa, respectively; flow stresses (average of the yield and tensile strengths), $\sigma_0$, were ~1016 MPa and ~800 MPa, and the failure strains, $\varepsilon_f$, were ~46% and ~47% respectively. (These are average values from two tensile tests on each alloy. Due to the premature failure in the grip region of one of the CrMnFeCoNi samples, a flow stress of $\sigma_0$ = 815 MPa has been used to construct the blunting line for the fracture toughness evaluation.)
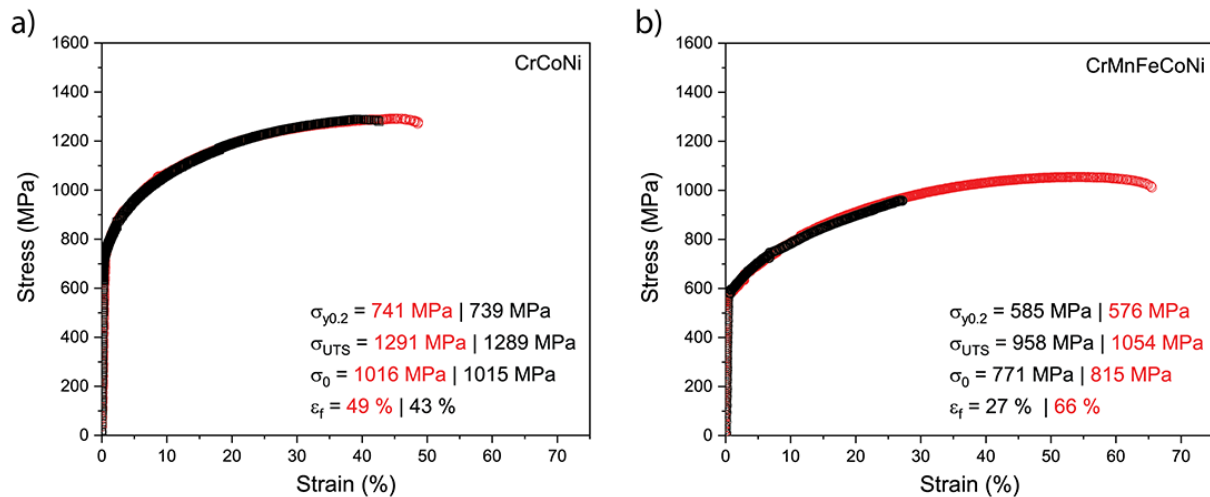


**Supplementary Fig. S4.** Tensile stress-strain curves and corresponding strength and ductility data of the (a) CrCoNi alloy and (b) CrMnFeCoNi alloy tested at 20 K.

Fracture Mechanics Testing

We used nonlinear-elastic fracture mechanics methods, which incorporate both the elastic and inelastic contributions, to measure the fracture toughness; specifically, the change in crack resistance with crack extension, *i.e.*, crack-resistance curve (*R*-curve) behavior, was characterized in terms of the *J*-integral as a function of crack growth primarily at 20 K but also at 293 K (room temperature) for comparison. Prior fracture toughness measurements in these alloys at 293 K, 198 K, and 77 K are also included in the paper for comparison; these have been described in detail elsewhere [10, 15]. The measurements at 20 K were performed at ENGIN-X, as described above.

Samples were tested under displacement control at a constant displacement rate of 2 mm/min. The onset of cracking as well as subsequent subcritical crack growth were determined by the compliance method with periodically unloading the sample (~10% of the peak-load) to record the elastic unloading compliance using a clip gauge of 3 mm (-1/+7 mm) gauge length (Epsilon Technology, Jackson, WY, USA) mounted in the load-line of the sample. Crack lengths, $a_i$ were calculated from the compliance data obtained during the test using the compliance expression of a C(T) sample at the load-line [17]:

$$\frac{a_i}{W} = 1.000196 - 4.06319u + 11.242u^2 - 106.043u^3 + 464.335u^4 - 650.677u^5 , \tag{3}$$

where

$$u = \frac{1}{[BEC_{c(i)}]^{\frac{1}{2}}+1} . \tag{4}$$

In Eq. 4, $C_{c(i)}$ is the rotation-corrected, elastic-unloading compliance and $B$ is the sample thickness. Initial and final crack lengths were also verified using optical measurements. For each crack length data point, $a_i$, the corresponding $J_i$-integral was computed as the sum of elastic, $J_{el\,(i)}$, and plastic components, $J_{pl\,(i)}$, such that the *J*-integral can be expressed as follows:

$$J_i = K_i^2/E' + J_{pl\,(i)} , \tag{5}$$

where $E' = E$, the Young's modulus, in plane stress and $E/(1-\nu^2)$ in plane strain; $\nu$ is Poisson's ratio. $K_i$, the linear-elastic stress intensity corresponding to each data point on the load-displacement curve, was calculated following:

$$K_i = \frac{P_i}{(B^2 W)^{\frac{1}{2}}} f(a_i/W) \ , \tag{6}$$

where $P_i$ is the applied load at each individual data point and $f(a_i/W)$ is a geometry-dependent function of the ratio of crack length, $a_i$, to width, $W$, as listed in the ASTM standard. The plastic component of $J_i$ can be calculated from the following equation:

$$J_{pl(i)} = \left[ J_{pl(i-1)} + \left( \frac{\eta_{pl(i-1)}}{b_{(i-1)}} \right) \frac{A_{pl(i)} - A_{pl(i-1)}}{B_N} \right] \left[ 1 - \gamma_{(i-1)} \left( \frac{a_{(i)} - a_{(i-1)}}{b_{(i-1)}} \right) \right] \ , \tag{7}$$

where $\eta_{pl\,(i-1)} = 2 + 0.522\, b_{(i-1)}/W$ and $\gamma_{pl\,(i-1)} = 1 + 0.76\, b_{(i-1)}/W$. $A_{pl\,(i)} - A_{pl\,(i-1)}$ is the increment of plastic area underneath the load-displacement curve, and $b_i$ is the uncracked ligament width (i.e., $b_i = W - a_i$). Following the above approach, the value of $J_i$ at any point along the load-displacement curve can be determined; along with the corresponding crack lengths, the $J$-$\Delta a$ resistance curve can then be constructed, where $\Delta a$ is the difference of the individual crack lengths, $a_i$, during crack growth and the initial crack length, $a$, after pre-cracking.

A provisional toughness $J_Q$ can be defined by the intersection of the resistance curve with the 0.2 mm offset/blunting line ($J = 2\,\sigma_o \Delta a$; where $\sigma_o$ is the effective flow stress). This provisional toughness $J_Q$ can be considered as a size-independent fracture toughness, $J_{Ic}$, provided the size requirements for $J$-field dominance and plane-strain conditions are met, i.e., respectively that $b_0$, $B > 10\, J_Q\,/\,\sigma_0$, where $b_0$ is the initial ligament length. The fracture toughness, $K_{JIc}$, expressed in terms of the stress intensity then can be obtained using the standard $J$-$K$ equivalence (mode I) relationship $K_{JIc} = (E'\, J_{Ic})^{1/2}$.

In terms of these ASTM specimen size criteria, all the fracture toughness values of the 5-component alloy at all temperatures, and the 3-component alloy at 293 to 77 K, fully conform to ASTM E1820 criteria for $J$-dominance and fully plane-strain conditions [17]. Specifically, for CrMnFeCoNi at 20 K, where the effective flow stress $\sigma_o$ that we measured was 815 MPa, the calculated values of the critical dimension, $10\, J_Q\,/\,\sigma_o$, were 3.7 mm and 9 mm for the initiation and growth toughnesses, respectively. For CrCoNi at 20 K, $\sigma_o = 1016$ MPa such that these critical dimensions were respectively 7.9 mm and 11 mm. This meant that although the crack-initiation toughness satisfied the criterion for $J$-dominance, it did not quite meet the criterion for fully plane-strain fracture. The crack-growth $K_{ss}$ toughnesses at 20 K were so large that they also did not meet

the 10 $J_Q$ / $\sigma_o$ criteria. However, we believe that the numbers for $K_{JIc}$ that we determined at crack initiation are close to a sample size-independent fracture toughness as the conditions for a *J*-dominant crack tip field were fully satisfied with an initial ligament length, $b_0$ of ~9 mm. Additional evidence for this is the lack of an upward ("concave-up") trend in the *R*-curve which can often be observed in samples that are tested under large-scale yielding conditions.

The temperature-dependent values of *E* and *ν* used in this study are from the measurements of Haglund et al. [55] for CrMnFeCoNi and Laplanche et al. [56] for CrCoNi. In the former study, data were obtained from 300 K down to 55 K, whereas those in the latter study were obtained from 1000 K down to 293 K. To obtain elastic constants at cryogenic temperatures outside these ranges, we fitted Varshni's [57] equation [$c_{ij}^0(T) = c_{ij}^0 - s/(e^{\frac{t}{T}} - 1)$] to the experimental data in the above papers [55, 56] and extrapolated to lower temperatures (in Varshni's equation $c_{ij}^0(T)$ and $c_{ij}^0$ are values of the elastic constants at temperature *T* and 0 K, respectively, and *s* and *t* are fitting constants). For CrMnFeCoNi [58], *s* and *t* for *E* are 35 GPa and 416 K, while those for *G* (shear modulus) are 16 GPa and 448 K; for CrCoNi [56], *s* and *t* for *E* are 32 GPa and 362 K, and 11.9 GPa and 362 K for *G*. Assuming isotropic elasticity: $\nu = \frac{E}{2G} - 1$. In this way, values for Young's moduli, *E*, at 293 K, 198 K, 77 K and 20 K, of 202 GPa, 209 GPa, 214.5, GPa and 214 GPa and Poisson's ratios, *ν*, of 0.266, 0.263, 0.256 and 0.259 were obtained for the CrMnFeCoNi alloy. Corresponding values were obtained for the CrCoNi alloy, namely, *E* = 229 GPa, 235 GPa, 241 GPa and 241 GPa and ν = 0.31, 0.30, 0.30 and 0.287 at 293 K, 198 K, 77 K and 20 K, respectively.

Characterization of Deformation and Fracture

After testing, the broken samples were immersed in acetone to prevent oxidation and then stored *in vacuo*. Fractographic analysis was performed with scanning electron microscopy using an FEI Strata DB235 SEM (FEI Company, Portland, OR, USA) operated in the secondary electron (SE) imaging mode at 5-15 kV, to identify the salient deformation and fracture mechanisms involved in the fracture.

To examine the microstructure and nature of the deformation mechanisms in the vicinity of, and remote from, the crack tip, the fractured samples were sectioned in two, each with a thickness of ~*B*/2, so that the crack-path profile in the plane-strain region in the interior of the sample could

be analyzed. For each sample, one half was embedded in conductive resin, progressively polished to a 0.05 μm surface finish, and finally vibration polished for 12 h in colloidal silica. The microstructure along the crack wake and the crack-tip region was then characterized using electron back-scattered diffraction (EBSD) in an FEI Strata DB235 SEM (FEI Company, Portland, OR, USA) operated at 20 kV using a TEAM EBSD analysis system (Ametek EDAX, Mahwah, NJ, USA) at 35 nm.

Transmission electron microscopy (TEM) was carried out to characterize the defect structures in the vicinity of the crack. Site-specific TEM foil samples were cut from the fractured samples and thinned to electron transparency using focused ion beam (FIB) milling (FEI, Helios G4 UX). Samples were trenched from regions both near the crack tip and far away from the deformed region from test specimens that were tested at both cryogenic and room temperature. High-resolution transmission electron microscopy (HRTEM) was conducted on an FEI ThemIS 60-300 STEM/TEM operated at 300 kV to investigate the deformation microstructure after fracture toughness testing at room and 20 K. Figure S5 shows an example of diffraction contrast imaging of the deformation features in the CrCoNi sample deformed at 293 K. 4D-STEM imaging of samples was conducted on the double-corrected TEAM I microscope and the FEI TitanX microscope (operated at 300 kV) at the National Center for Electron Microscopy (NCEM, LBNL). A 1 mrad bullseye aperture was used with an electron probe size of approximately 1.5 nm on the TEAM1 and 2 nm on the TitanX. The scanning step size was set to 1.5 nm, accordingly. Figure S6 shows 4D-STEM analysis of the CrMnFeCoNi alloy deformed at 20 K.
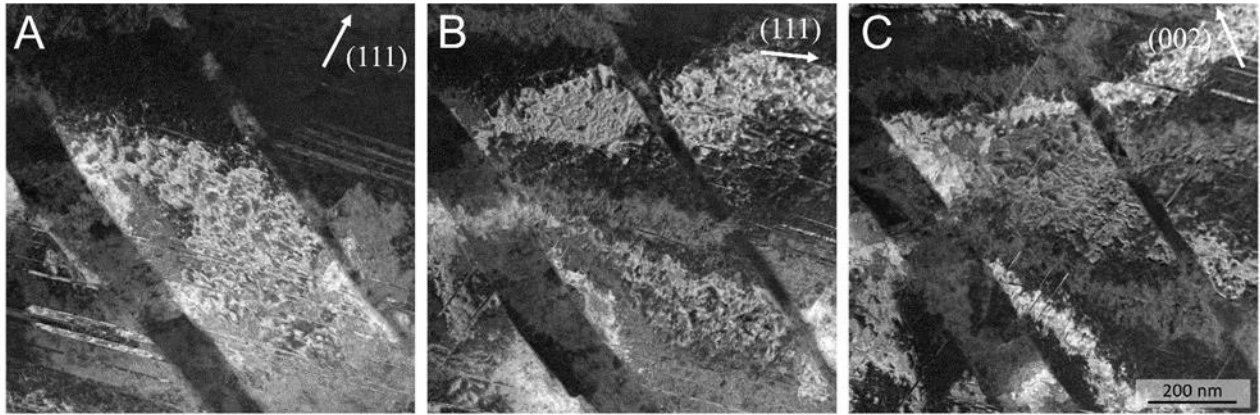
**Supplementary Fig. S5.** Diffraction contrast imaging (DCI) in STEM mode for the sample deformed and fractured at 293 K with three different two-beam conditions indicated by the white arrows. A relatively high density of dislocations can be identified in between the planar deformation bands.
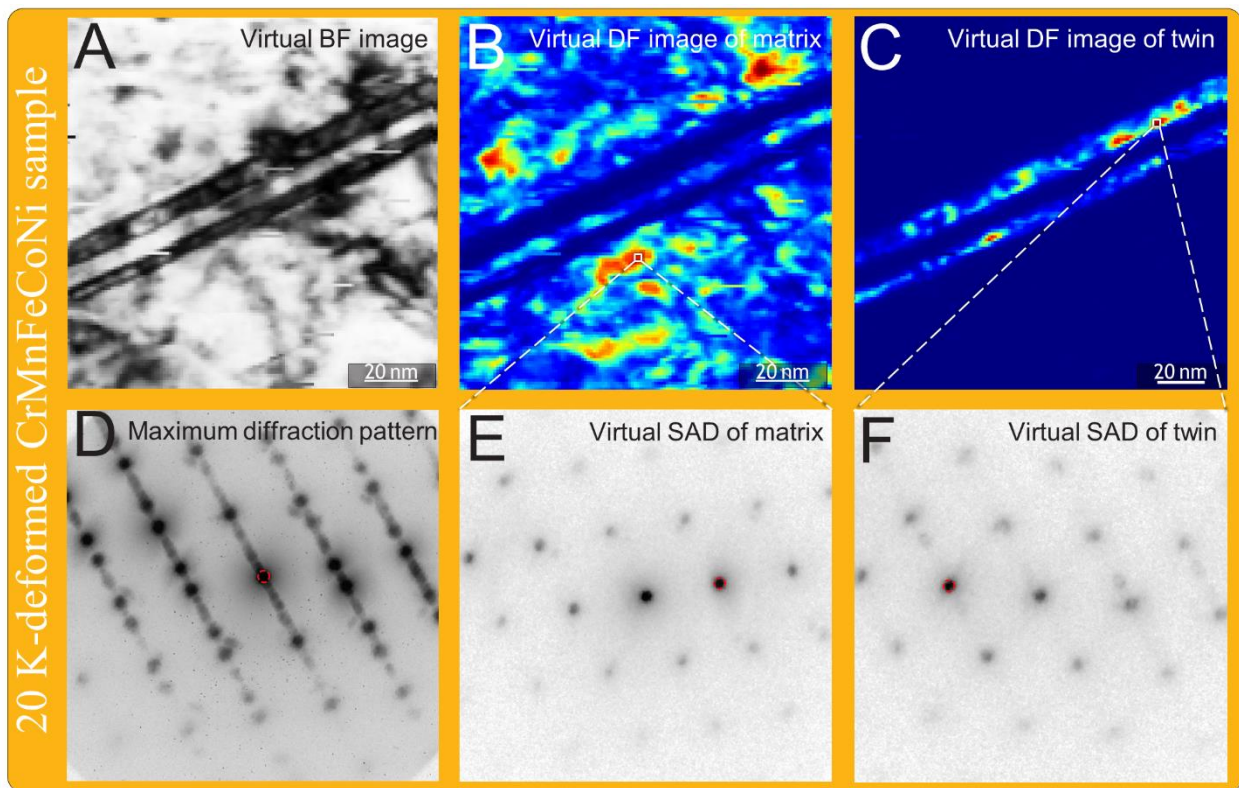


**Supplementary Fig. S6. 4D-STEM characterization of the deformed microstructure in the CrMnFeCoNi alloy adjacent to the 20 K fracture surface, showing nano-twin features.** (A-C) are virtual images from the 4D-STEM dataset and (D-F) are selected diffraction patterns from the same data set taken from the [110] orientation. (A) Virtual bright-field image generated from the 4D-STEM scan. The virtual aperture was placed at the (000) beam, as shown by the red circle in (D). (B) Virtual dark-field image using a [111] matrix reflection as shown in (E). (C) virtual dark-field image using a [200] twin reflection as shown with the red circle in (F).

Lattice parameters and peak broadening in neutron diffraction

Time-of-flight (ToF) neutron diffraction spectra collected for single phase *fcc* ternary CrCoNi material with the ToF axis being converted into interplanar *d*-spacing in Å (fig. S7a), shows the spectral evolution with cooling from 293 K down to cryogenic temperatures of 20 K and increasing the load from 10% to 75% of the maximum load. A clear peak shift in the crystal planes can be seen in both graphs as a result of cooling as well as loading. Dashed straight lines and different solid line colors in fig. S7a and b are for visual guidance only. Note that despite the fact that the TEM results in the present work (Fig. 4) did reveal limited evidence of the formation of the *hcp* phase in the CrCoNi alloy, our *in situ* neutron diffraction measurements did not. Of note here is that He et al. [45] reported the formation of 4 vol.% of *hcp* phase based on the (101) peak in neutron diffraction spectra collected from a uniaxial tensile specimen tested at 15 K with a strain between 14% and 30%. However, in the present work, the highly strained volume ahead of the crack tip within the plastic zone is more than an order of magnitude smaller compared with a uniaxial tension configuration. With a 4x4x4 mm³ instrumental gauge volume used in the neutron measurement, the small fraction of *hcp* phase did not yield a sufficient diffraction signal discernable in the overall spectrum, although a broadening of the (200) and (111) peaks, similar to that reported in He et al.'s work [45], was detected.

The lattice constant $a_0$ for the single phase *fcc* ternary CrCoNi alloy at 293 K was determined to be 3.56 Å by fitting the {200} peak position (half of the {100}) from the diffraction spectra collected at 293 K. These data were compared with several literature values listed in fig. S7c and a good consistency can be seen. The lattice strain $\varepsilon_{hkl}$ was calculated based on the *{hkl}* planes interplanar spacing $d_{hkl}$ fitted by the Pseudo Voigt profile in a dedicated ENGIN-X's Script Based Analysis programme EX-SBA, by following the relationship:

$$\varepsilon_{hkl} \frac{\left(d^i_{hkl} - d^0_{hkl}\right)}{d^0_{hkl}} \quad . \tag{8}$$

Here $d_{hkl}^i$ is the lattice spacing of *{hkl}* plane when material is stressed at each load step (*i*) where the ToF neutron diffraction scan was acquired and $d_{hkl}^0$ is the value for the stress-free material. Further, the polycrystalline coefficient of thermal expansion (CTE) $\alpha_{hkl}$ for the *fcc* CrCoNi alloy in specific *{hkl}* crystallographic planes due to thermal shrinkage at each cooling step was calculated from:

$$\alpha_{hkl} = \frac{\varepsilon_{hkl}}{\Delta T^i} = \frac{\left(d_{hkl}^i - d_{hkl}^0\right)}{d_{hkl}^0 \times (T^i - T^0)} \tag{9}$$

where $\Delta T^i$ is the temperature difference between each cooling temperature step ($T^i$) and initial reference temperature ($T^0$).

As shown in fig. S7d, cooling from room temperature to 20 K introduced increasing strains to the crystal lattice; the values derived for {200}, {400}, {111} and {222} planes are similar following an exponential increase with a plateau towards a lower temperature. The coefficient of thermal expansion (CTE) was derived and is shown in fig. S7e. The CTE at room temperature was determined to be 22.9±1.8 × $10^{-6}$/K for planes in the direction of <200> and 19.8±2.0 ×$10^{-6}$/K for the <111> direction. These values are in a similar range as the average CTE values for polycrystalline CrCoNi measured by Laplanche et al. ~13×$10^{-6}$/K [56], and Moravcik et al. 17.4×$10^{-6}$/K [59]. We determined the CTE at 20 K to be 8.0±0.2 ×$10^{-6}$/K for <200> direction and 7.8±0.3 ×$10^{-6}$/K for <111> direction; there are no open published data in the literature at this temperature to compare with our present results. Lattice strains at 20 K were further increased under increasing load. However, the load-induced lattice strains were different even on the same family of planes, e.g., the {200} and {400} planes showed different strains. This is consistent with that reported by Wang et al. [54] and Naeem et al. [25]. Since {200} and {400} planes are equivalent plane families, as are {111} and {222}, differences in their lattice strains in the same family due to loading indicates additional potential straining introduced by stacking faults as described by Wang et al. [54] and Naeem et al. [25]. Note that there is no difference in their strains due to cooling (fig. S7d), indicating that temperature change alone did not introduce stacking faults. Using the methodology adopted in refs. 25 and 55, the highest stacking-fault probability (SFP) in the current CrCoNi material under load at 20 K was found to be about 6.3×$10^{-3}$; we could not assign an exact strain value to this SFP

as the true stress in the instrumental gauge volume ahead of the crack tip is non-uniform varying from high values in the small volume ahead of the crack tip to low levels further away from the crack.

Lastly, as mentioned earlier, peak broadening was observed, as shown by the Pseudo Voigt profile fitted Full Width at Half Maximum (FWHM) of the diffraction peaks (200) and (111) planes in the CrCoNi alloy when plotted as a function of the applied load. Consistent with the lattice strain measurement, the insert in fig. S7f shows no evidence of any cooling-induced peak broadening in (200) and (111). However, at 20 K when load was applied, the FWHM of the (200) and (111) planes in the CrCoNi alloy demonstrated a gradual increase with increasing load, indicating the introduction of defects as predicted from the lattice strain measurements; specifically, peak broadening of up to 60% was apparent when the load reached ~80% of the maximum load (fig. S7h). Similar trends (not shown) were observed in the CrMnFeCoNi alloy.
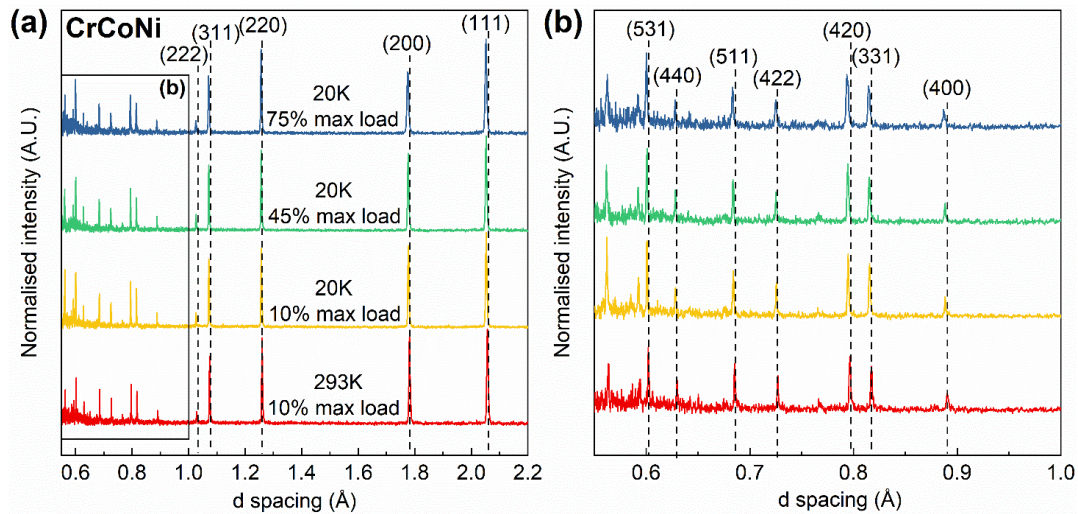


| Lattice constant $a_0$ (Å) at RT | Method | Authors |
|---|---|---|
| 3.559 | Pair distribution function (PDF) | Zhang et al. 2017 [60] |
| 3.563 | DFT computation | Yin et al. 2020 [61] |
| 3.565 | XRD | Moravcik et al. 2017 [59] |
| 3.56 | XRD | Lee et al. 2019 [62] |
| 3.567 | XRD | Laplanche et al. 2017 [63] |
| 3.57 | XRD | Laplanche et al. 2018 [56] |
| **3.562** | **neutron diffraction** | **Present work** |
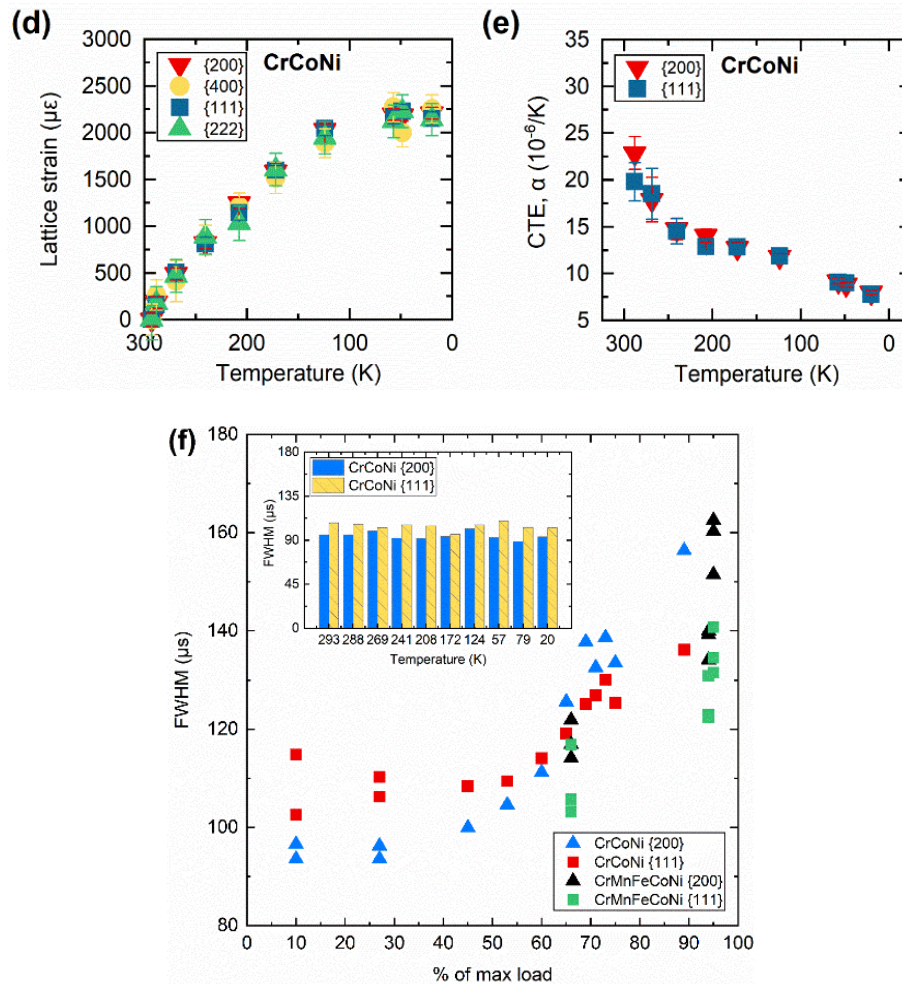
**Supplementary Fig. S7. (a)** Typical examples of ToF neutron diffraction spectra acquired for CrCoNi. Bragg diffraction peaks corresponding to different crystallographic planes have been labeled with *(hkl)*. The magnified view of the lower *d*-spacing planes (in the range of 0.55 to 1 Å) in (a) is plotted in (b) resolved by the dedicated ENGIN-X diffractometer. (c) The measured single phase *fcc* lattice constant $a_0$ in CrCoNi material is 3.562 Å at room temperature and compared to various literature values obtained by experiments or simulations. (d) The calculated lattice strain of {200}, {400}, {111} and {222} planes due to thermal cooling are plotted as a function of temperature. (e) Calculated polycrystalline coefficient of thermal expansion (CTE) as a function of the temperature decrease. (f) Pseudo Voigt profile fitted Full Width at Half Maximum (FWHM) of the diffraction peaks {200} and {111} planes in CrCoNi and CrMnFeCoNi alloys plotted as a function of applied load, the insert in (f) plots CrCoNi diffraction peak FWHM with temperature, showing only loading impacts the peak broadening.

**References and Notes**

1. B. Cantor, I. T. H. Chang, P. Knight, A. J. B. Vincent, Microstructural development in equiatomic multicomponent alloys. *Mater. Sci. Eng. A* **375–377**, 213–218 (2004). [doi:10.1016/j.msea.2003.10.257](doi:10.1016/j.msea.2003.10.257)

2. J.-W. Yeh, S.-K. Chen, S.-J. Lin, J.-Y. Gan, T.-S. Chin, T.-T. Shun, C.-H. Tsau, S.-Y. Chang, Nanostructured high-entropy alloys with multiple principal elements: Novel alloy design concepts and outcomes. *Adv. Eng. Mater.* **6**, 299–303 (2004). [doi:10.1002/adem.200300567](doi:10.1002/adem.200300567)

3. E. P. George, W. A. Curtin, C. C. Tasan, High entropy alloys: A focused review of mechanical properties and deformation mechanisms. *Acta Mater.* **188**, 435–474 (2020). [doi:10.1016/j.actamat.2019.12.015](doi:10.1016/j.actamat.2019.12.015)

4. E. J. Pickering, N. G. Jones, High-entropy alloys: A critical assessment of their founding principles and future prospects. *Int. Mater. Rev.* **61**, 183–202 (2016). [doi:10.1080/09506608.2016.1180020](doi:10.1080/09506608.2016.1180020)

5. D. B. Miracle, O. N. Senkov, A critical review of high entropy alloys and related concepts. *Acta Mater.* **122**, 448–511 (2017). [doi:10.1016/j.actamat.2016.08.081](doi:10.1016/j.actamat.2016.08.081)

6. Z. Li, S. Zhao, R. O. Ritchie, M. A. Meyers, Mechanical properties of high-entropy alloys with emphasis on face-centered cubic alloys. *Prog. Mater. Sci.* **102**, 296–345 (2019). [doi:10.1016/j.pmatsci.2018.12.003](doi:10.1016/j.pmatsci.2018.12.003)

7. E. P. George, D. Raabe, R. O. Ritchie, High-entropy alloys. *Nat. Rev. Mater.* **4**, 515–534 (2019). [doi:10.1038/s41578-019-0121-4](doi:10.1038/s41578-019-0121-4)

8. A. Gali, E. P. George, Tensile properties of high- and medium-entropy alloys. *Intermetallics* **39**, 74–78 (2013). [doi:10.1016/j.intermet.2013.03.018](doi:10.1016/j.intermet.2013.03.018)

9. F. Otto, A. Dlouhý, Ch. Somsen, H. Bei, G. Eggeler, E. P. George, The influences of temperature and microstructure on the tensile properties of a CoCrFeMnNi high-entropy alloy. *Acta Mater.* **61**, 5743–5755 (2013). [doi:10.1016/j.actamat.2013.06.018](doi:10.1016/j.actamat.2013.06.018)

10. B. Gludovatz, A. Hohenwarter, D. Catoor, E. H. Chang, E. P. George, R. O. Ritchie, A fracture-resistant high-entropy alloy for cryogenic applications. *Science* **345**, 1153–1158 (2014). [doi:10.1126/science.1254581](doi:10.1126/science.1254581) [Medline](Medline)

11. S. Zhao, Z. Li, C. Zhu, W. Yang, Z. Zhang, D. E. J. Armstrong, P. S. Grant, R. O. Ritchie, M. A. Meyers, Amorphization in extreme deformation of the CrMnFeCoNi high-entropy alloy. *Sci. Adv.* **7**, eabb3108 (2021). [doi:10.1126/sciadv.abb3108](doi:10.1126/sciadv.abb3108) [Medline](Medline)

12. Z. Li, K. G. Pradeep, Y. Deng, D. Raabe, C. C. Tasan, Metastable high-entropy dual-phase alloys overcome the strength-ductility trade-off. *Nature* **534**, 227–230 (2016). [doi:10.1038/nature17981](doi:10.1038/nature17981) [Medline](Medline)

13. F. Da Costa Garcia Filho, R. O. Ritchie, M. A. Meyers, S. Neves Monteiro, Cantor-derived medium-entropy alloys: Bridging the gap between traditional metallic and high-entropy alloys. *J. Mater. Res. Technol.* **17**, 1868–1895 (2022). [doi:10.1016/j.jmrt.2022.01.118](doi:10.1016/j.jmrt.2022.01.118)

14. Z. Wu, H. Bei, G. M. Pharr, E. P. George, Temperature dependence of the mechanical properties of equiatomic solid solution alloys with face-centered cubic crystal structures. *Acta Mater.* **81**, 428–441 (2014). doi:10.1016/j.actamat.2014.08.026

15. B. Gludovatz, A. Hohenwarter, K. V. S. Thurston, H. Bei, Z. Wu, E. P. George, R. O. Ritchie, Exceptional damage-tolerance of a medium-entropy alloy CrCoNi at cryogenic temperatures. *Nat. Commun.* **7**, 10602 (2016). doi:10.1038/ncomms10602 Medline

16. R. O. Ritchie, The conflicts between strength and toughness. *Nat. Mater.* **10**, 817–822 (2011). doi:10.1038/nmat3115 Medline

17. E08 Committee, ASTM E1820-17a Standard Test Method for Measurement of Fracture Toughness (ASTM International, 2017).

18. M. Yang, L. Zhou, C. Wang, P. Jiang, F. Yuan, E. Ma, X. Wu, High impact toughness of CrCoNi medium-entropy alloy at liquid-helium temperature. *Scr. Mater.* **172**, 66–71 (2019). doi:10.1016/j.scriptamat.2019.07.010

19. A. S. Tirunilai, J. Sas, K.-P. Weiss, H. Chen, D. V. Szabó, S. Schlabach, S. Haas, D. Geissler, J. Freudenberger, M. Heilmaier, A. Kauffmann, Peculiarities of deformation of CoCrFeMnNi at cryogenic temperatures. *J. Mater. Res.* **33**, 3287–3300 (2018). doi:10.1557/jmr.2018.252

20. J. Liu, X. Guo, Q. Lin, Zh. He, X. An, L. Li, P. K. Liaw, X. Liao, L. Yu, J. Lin, L. Xie, J. Ren, Y. Zhang, Excellent ductility and serration feature of metastable CoCrFeNi high-entropy alloy at extremely low temperatures. *Sci. China Mater.* **62**, 853–863 (2019). doi:10.1007/s40843-018-9373-y

21. A. S. Tirunilai, T. Hanemann, K.-P. Weiss, J. Freudenberger, M. Heilmaier, A. Kauffmann, Dislocation-based serrated plastic flow of high entropy alloys at cryogenic temperatures. *Acta Mater.* **200**, 980–991 (2020). doi:10.1016/j.actamat.2020.09.052

22. J. Moon, E. Tabachnikova, S. Shumilin, T. Hryhorova, Y. Estrin, J. Brechtl, P. K. Liaw, W. Wang, K. A. Dahmen, A. Zargaran, J. W. Bae, H.-S. Do, B.-J. Lee, H. S. Kim, Deformation behavior of a Co-Cr-Fe-Ni-Mo medium-entropy alloy at extremely low temperatures. *Mater. Today* **50**, 55–68 (2021). doi:10.1016/j.mattod.2021.08.001

23. Z. Zhang, M. M. Mao, J. Wang, B. Gludovatz, Z. Zhang, S. X. Mao, E. P. George, Q. Yu, R. O. Ritchie, Nanoscale origins of the damage tolerance of the high-entropy alloy CrMnFeCoNi. *Nat. Commun.* **6**, 10143 (2015). doi:10.1038/ncomms10143 Medline

24. Z. Zhang, H. Sheng, Z. Wang, B. Gludovatz, Z. Zhang, E. P. George, Q. Yu, S. X. Mao, R. O. Ritchie, Dislocation mechanisms and 3D twin architectures generate exceptional strength-ductility-toughness combination in CrCoNi medium-entropy alloy. *Nat. Commun.* **8**, 14390 (2017). doi:10.1038/ncomms14390 Medline

25. M. Naeem, H. He, F. Zhang, H. Huang, S. Harjo, T. Kawasaki, B. Wang, S. Lan, Z. Wu, F. Wang, Y. Wu, Z. Lu, Z. Zhang, C. T. Liu, X.-L. Wang, Cooperative deformation in high-entropy alloys at ultralow temperatures. *Sci. Adv.* **6**, eaax4002 (2020). doi:10.1126/sciadv.aax4002 Medline

26. M. Kawamura, M. Asakura, N. L. Okamoto, K. Kishida, H. Inui, E. P. George, Plastic deformation of single crystals of the equiatomic Cr−Mn−Fe−Co−Ni high-entropy alloy in tension and compression from 10 K to 1273 K. *Acta Mater.* **203**, 116454 (2021). [doi:10.1016/j.actamat.2020.10.073](doi:10.1016/j.actamat.2020.10.073)

27. L. Li, Z. Chen, S. Kuroiwa, M. Ito, K. Kishida, H. Inui, E. P. George, Tensile and compressive plastic deformation behavior of medium-entropy Cr-Co-Ni single crystals from cryogenic to elevated temperatures. *Int. J. Plast.* **148**, 103144 (2022). [doi:10.1016/j.ijplas.2021.103144](doi:10.1016/j.ijplas.2021.103144)

28. L. Tang, K. Yan, B. Cai, Y. Q. Wang, B. Liu, S. Kabra, M. M. Attallah, Y. Liu, Deformation mechanisms of FeCoCrNiMo$_{0.2}$ high entropy alloy at 77 and 15 K. *Scr. Mater.* **178**, 166–170 (2020). [doi:10.1016/j.scriptamat.2019.11.026](doi:10.1016/j.scriptamat.2019.11.026)

29. M. Shih, J. Miao, M. Mills, M. Ghazisaeidi, Stacking fault energy in concentrated alloys. *Nat. Commun.* **12**, 3590 (2021). [doi:10.1038/s41467-021-23860-z](doi:10.1038/s41467-021-23860-z) [Medline](Medline)

30. X. Sun, S. Lu, R. Xie, X. An, W. Li, T. Zhang, C. Liang, X. Ding, Y. Wang, H. Zhang, L. Vitos, Can experiment determine the stacking fault energy of metastable alloys? *Mater. Des.* **199**, 109396 (2021). [doi:10.1016/j.matdes.2020.109396](doi:10.1016/j.matdes.2020.109396)

31. K. V. Werner, F. Niessen, M. Villa, M. A. J. Somers, Experimental validation of negative stacking fault energies in metastable face-centered cubic materials. *Appl. Phys. Lett.* **119**, 141902 (2021). [doi:10.1063/5.0063761](doi:10.1063/5.0063761)

32. E. P. George, R. O. Ritchie, High-entropy materials. *MRS Bull.* **47**, 145–150 (2022). [doi:10.1557/s43577-022-00285-7](doi:10.1557/s43577-022-00285-7)

33. G. Laplanche, A. Kostka, O. M. Horst, G. Eggeler, E. P. George, Microstructure evolution and critical stress for twinning in the CrMnFeCoNi high-entropy alloy. *Acta Mater.* **118**, 152–163 (2016). [doi:10.1016/j.actamat.2016.07.038](doi:10.1016/j.actamat.2016.07.038)

34. K. V. S. Thurston, A. Hohenwarter, G. Laplanche, E. P. George, B. Gludovatz, R. O. Ritchie, On the onset of deformation twinning in the CrFeMnCoNi high-entropy alloy using a novel tensile specimen geometry. *Intermetallics* **110**, 106469 (2019). [doi:10.1016/j.intermet.2019.04.012](doi:10.1016/j.intermet.2019.04.012)

35. A. C. Mackenzie, J. W. Hancock, D. K. Brown, On the influence of state of stress on ductile failure initiation in high strength steels. *Eng. Fract. Mech.* **9**, 167–188 (1977). [doi:10.1016/0013-7944(77)90062-5](doi:10.1016/0013-7944(77)90062-5)

36. R. O. Ritchie, A. W. Thompson, On macroscopic and microscopic analyses for crack initiation and crack growth toughness in ductile alloys. *Metall. Mater. Trans. A* **16**, 233–248 (1985). [doi:10.1007/BF02816050](doi:10.1007/BF02816050)

37. J. Miao, C. E. Slone, T. M. Smith, C. Niu, H. Bei, M. Ghazisaeidi, G. M. Pharr, M. J. Mills, The evolution of the deformation substructure in a Ni-Co-Cr equiatomic solid solution alloy. *Acta Mater.* **132**, 35–48 (2017). [doi:10.1016/j.actamat.2017.04.033](doi:10.1016/j.actamat.2017.04.033)

38. B. Schuh, B. Völker, J. Todt, K. S. Kormout, N. Schell, A. Hohenwarter, Influence of annealing on microstructure and mechanical properties of a nanocrystalline CrCoNi medium-entropy alloy. *Materials* **11**, 662 (2018). [doi:10.3390/ma11050662](doi:10.3390/ma11050662) [Medline](Medline)

39. S. Chen, H. S. Oh, B. Gludovatz, S. J. Kim, E. S. Park, Z. Zhang, R. O. Ritchie, Q. Yu, Real-time observations of TRIP-induced ultrahigh strain hardening in a dual-phase CrMnFe-CoNi high-entropy alloy. *Nat. Commun.* **11**, 826 (2020). [doi:10.1038/s41467-020-14641-1](doi:10.1038/s41467-020-14641-1) [Medline](Medline)

40. Q. Lin, J. Liu, X. An, H. Wang, Y. Zhang, X. Liao, Cryogenic-deformation-induced phase transformation in an FeCoCrNi high-entropy alloy. *Mater. Res. Lett.* **6**, 236–243 (2018). [doi:10.1080/21663831.2018.1434250](doi:10.1080/21663831.2018.1434250)

41. C. Niu, C. R. LaRosa, J. Miao, M. J. Mills, M. Ghazisaeidi, Magnetically-driven phase transformation strengthening in high entropy alloys. *Nat. Commun.* **9**, 1363 (2018). [doi:10.1038/s41467-018-03846-0](doi:10.1038/s41467-018-03846-0) [Medline](Medline)

42. Z. Dong, S. Schönecker, W. Li, D. Chen, L. Vitos, Thermal spin fluctuations in CoCrFeMnNi high entropy alloy. *Sci. Rep.* **8**, 12211 (2018). [doi:10.1038/s41598-018-30732-y](doi:10.1038/s41598-018-30732-y) [Medline](Medline)

43. P.-A. Dubos, J. Fajoui, N. Iskounen, M. Coret, S. Kabra, J. Kelleher, B. Girault, D. Gloaguen, Temperature effect on strain-induced phase transformation of cobalt. *Mater. Lett.* **281**, 128812 (2020). [doi:10.1016/j.matlet.2020.128812](doi:10.1016/j.matlet.2020.128812)

44. L. Rémy, A. Pineau, Twinning and strain-induced f.c.c.→h.c.p. transformation on the mechanical properties of Co–Ni–Cr–Mo alloys. *Mater. Sci. Eng.* **26**, 123–132 (1976). [doi:10.1016/0025-5416(76)90234-2](doi:10.1016/0025-5416(76)90234-2)

45. H. He, M. Naeem, F. Zhang, Y. Zhao, S. Harjo, T. Kawasaki, B. Wang, X. Wu, S. Lan, Z. Wu, W. Yin, Y. Wu, Z. Lu, J.-J. Kai, C. T. Liu, X.-L. Wang, Stacking fault driven phase transformation in CrCoNi medium entropy alloy. *Nano Lett.* **21**, 1419–1426 (2021). [doi:10.1021/acs.nanolett.0c04244](doi:10.1021/acs.nanolett.0c04244) [Medline](Medline)

46. J. Ding, Q. Yu, M. Asta, R. O. Ritchie, Tunable stacking fault energies by tailoring local chemical order in CrCoNi medium-entropy alloys. *Proc. Natl. Acad. Sci. U.S.A.* **115**, 8919–8924 (2018). [doi:10.1073/pnas.1808660115](doi:10.1073/pnas.1808660115) [Medline](Medline)

47. P. Yu, J.-P. Du, S. Shinzato, F.-S. Meng, S. Ogata, Theory of history-dependent multi-layer generalized stacking fault energy— A modeling of the micro-substructure evolution kinetics in chemically ordered medium-entropy alloys. *Acta Mater.* **224**, 117504 (2022). [doi:10.1016/j.actamat.2021.117504](doi:10.1016/j.actamat.2021.117504)

48. R. Zhang, S. Zhao, J. Ding, Y. Chong, T. Jia, C. Ophus, M. Asta, R. O. Ritchie, A. M. Minor, Short-range order and its impact on the CrCoNi medium-entropy alloy. *Nature* **581**, 283–287 (2020). [doi:10.1038/s41586-020-2275-z](doi:10.1038/s41586-020-2275-z) [Medline](Medline)

49. H. S. Oh, K. Odbadrakh, Y. Ikeda, S. Mu, F. Körmann, C.-J. Sun, H. S. Ahn, K. N. Yoon, D. Ma, C. C. Tasan, T. Egami, E. S. Park, Element-resolved local lattice distortion in complex concentrated alloys: An observable signature of electronic effects. *Acta Mater.* **216**, 117135 (2021). [doi:10.1016/j.actamat.2021.117135](doi:10.1016/j.actamat.2021.117135)

50. T. S. Byun, T. G. Lach, "Mechanical Properties of 304L and 316L Austenitic Stainless Steels after Thermal Aging for 1500 Hours," Pacific Northwest National Laboratory Report, US Department of Energy, PNNL-25854, M3LW-16OR040215 (2016).

51. R. M. McClintock, H. P. Gibbons, *Mechanical Properties of Structural Materials: A Compilation from the Literature*, National Bureau of Standards Monograph 13 (US Department of Commerce, National Bureau of Standards, 1960).

52. B. Gludovatz, E. P. George, R. O. Ritchie, Processing, microstructure and mechanical properties of the CrMnFeCoNi high-entropy alloy. *J. Miner. Met. Mater. Soc.* **67**, 2262–2270 (2015). doi:10.1007/s11837-015-1589-z

53. O. Kirichek, J. D. Timms, J. F. Kelleher, R. B. E. Down, C. D. Offer, S. Kabra, S. Y. Zhang, Sample environment for neutron scattering measurements of internal stresses in engineering materials in the temperature range of 6 K to 300 K. *Rev. Sci. Instrum.* **88**, 025103 (2017). doi:10.1063/1.4974815 Medline

54. Y. Q. Wang, B. Liu, K. Yan, M. S. Wang, S. Kabra, Y. L. Chiu, D. Dye, P. D. Lee, Y. Liu, B. Cai, Probing deformation mechanisms of a FeCoCrNi high-entropy alloy at 293 and 77 K using *in situ* neutron diffraction. *Acta Mater.* **163**, 240–242 (2019). doi:10.1016/j.actamat.2018.10.010

55. A. Haglund, M. Koehler, D. Catoor, E. P. George, V. Keppens, Polycrystalline elastic moduli of a high-entropy alloy at cryogenic temperatures. *Intermetallics* **58**, 62–64 (2015). doi:10.1016/j.intermet.2014.11.005

56. G. Laplanche, P. Gadaud, C. Bärsch, K. Demtröder, C. Reinhart, J. Schreuer, E. P. George, Elastic moduli and thermal expansion coefficients of medium-entropy subsystems of the CrMnFeCoNi high-entropy alloy. *J. Alloys Compd.* **746**, 244–255 (2018). doi:10.1016/j.jallcom.2018.02.251

57. Y. P. Varshni, Temperature dependence of the elastic constants. *Phys. Rev. B* **2**, 3952–3958 (1970). doi:10.1103/PhysRevB.2.3952

58. G. Laplanche, P. Gadaud, O. Horst, F. Otto, G. Eggeler, E. P. George, Temperature dependencies of the elastic moduli and thermal expansion coefficient of an equiatomic, single-phase CoCrFeMnNi high-entropy alloy. *J. Alloys Compd.* **623**, 348–353 (2015). doi:10.1016/j.jallcom.2014.11.061

59. I. Moravcik, J. Cizek, Z. Kovacova, J. Nejezchlebova, M. Kitzmantel, E. Neubauer, I. Kubena, V. Hornik, I. Dlouhy, Mechanical and microstructural characterization of powder metallurgy CoCrNi medium entropy alloy. *Mater. Sci. Eng. A* **701**, 370–380 (2017). doi:10.1016/j.msea.2017.06.086

60. F. X. Zhang, S. Zhao, K. Jin, H. Xue, G. Velisa, H. Bei, R. Huang, J. Y. P. Ko, D. C. Pagan, J. C. Neuefeind, W. J. Weber, Y. Zhang, Local structure and short-range order in a NiCoCr solid solution alloy. *Phys. Rev. Lett.* **118**, 205501 (2017). doi:10.1103/PhysRevLett.118.205501 Medline

61. B. Yin, S. Yoshida, N. Tsuji, W. A. Curtin, Yield strength and misfit volumes of NiCoCr and implications for short-range-order. *Nat. Commun.* **11**, 2507 (2020). doi:10.1038/s41467-020-16083-1 Medline

62. D. Lee, M. P. Agustianingrum, N. Park, N. Tsuji, Synergistic effect by Al addition in improving mechanical performance of CoCrNi medium-entropy alloy. *J. Alloys Compd.* **800**, 372–378 (2019). doi:10.1016/j.jallcom.2019.06.005

63. G. Laplanche, A. Kostka, C. Reinhart, J. Hunfeld, G. Eggeler, E. P. George, Reasons for the superior mechanical properties of medium-entropy CrCoNi compared to high-entropy CrMnFeCoNi. *Acta Mater.* **128**, 292–303 (2017). doi:10.1016/j.actamat.2017.02.036